Evoking C_{2+} Production from Electrochemical CO_2 Reduction by the Steric Confinement Effect of Ordered Porous Cu_2O

Longlong Fan,[a] Qinghong Geng,[a] Lian Ma,[a] Chengming Wang,[b] Jun-Xuan Li,[a] Wei Zhu,[a] Ruiwen Shao,[c] Wei Li,[d] Xiao Feng,[a] Yusuke Yamauchi,[e,f] Cuiling Li,*[a,b] and Lei Jiang[b,g,h]

[a] Key Laboratory of Cluster Science, Ministry of Education, Beijing Key Laboratory of Photoelectronic/Electrophotonic Conversion Materials, School of Chemistry and Chemical Engineering, Beijing Institute of Technology, Beijing 100081, China

[b] CAS Key Laboratory of Bio-Inspired Materials and Interface Science, Technical Institute of Physics and Chemistry, Chinese Academy of Sciences, Beijing 100190, China

E-mail: licuiling@bit.edu.cn; licuiling@mail.ipc.ac.cn

[c] Beijing Advanced Innovation Center for Intelligent Robots and Systems and Institute of Engineering Medicine, Beijing Institute of Technology, Beijing 100081, China

[d] Department of Chemistry, Laboratory of Advanced Materials, Shanghai Key Laboratory of Molecular Catalysis and Innovative Materials, iChEM and State Key Laboratory of Molecular Engineering of Polymers, Fudan University, Shanghai 200433, China

[e] School of Chemical Engineering and Australian Institute for Bioengineering and Nanotechnology (AIBN), The University of Queensland, Brisbane 4072, Australia

[f] JST-ERATO Yamauchi Materials Space-Tectonics Project and Department of Materials Process Engineering, Graduate School of Engineering, Nagoya University, Furo-cho, Chikusa-ku, Nagoya, Aichi, 464-8603, Japan

[g] Key Laboratory of Bio-Inspired Smart Interfacial Science and Technology of Ministry of Education, School of Chemistry, Beihang University, Beijing 100191, China

[h] School of Future Technology, University of Chinese Academy of Sciences, Beijing 101407, China

Experimental Procedures

Chemicals: Ammonium hydroxide ($NH_3 \cdot H_2O$, Aladdin Industrial Corporation Co., Ltd), potassium persulfate ($K_2S_2O_8$, 99 wt.%, J&K scientific Chemical Co.), styrene (99%, Macklin Co., Ltd.), sodium hydroxide pellets (NaOH, 96%, Aladdin Industrial Corporation Co., Ltd.), Nafion solution, Copper(II)Chloride Dihydrate, ascorbic acid, Polyvinylpyrrolidone K30 and Poloxamer were purchased from Sigma Aldrich. N,N-Dimethylformamide (DMF), ethanol and methanol were purchased from Shanghai Titan Scientific Co., Ltd. Ultrapure water (Milli-Q Integral 5, 18.0 MΩ·cm resistivity) was used in all experiments. All chemicals were used without further purification.

Preparation of polystyrene (PS) spheres. The PS spheres with diameter of 270 nm were synthesized according to previous literature.[1] In a typical synthesis, 70 mL of styrene was first washed thoroughly with 20 mL of 10 wt.% NaOH solution and deionized water (DI-water) successively to remove the stabilizer. Then, 65 mL of the washed styrene was added to a triple-neck, 1 L round bottomed flask with 500 mL water containing 2.5 g of PVP. After bubbling with nitrogen for 15 min, the mixture was then fluxed at 75 ˚C under magnetic stirring for 30 min. Subsequently, 50 mL of aqueous solution containing 1.0 g of $K_2S_2O_8$ was added quickly into the flask to initiate the polymerization reaction of styrene. After keeping stirring for 24 h at this temperature, the mixture was cooled down and the obtained milk-like product was the monodispersed colloidal polystyrene spheres. It was worthy to note that the rotation rate in polymerization step should keep at below 500 rpm, because higher rotation rate would lead to the agglomeration of PS template.

Preparation of 3D ordered PS template. The 3D ordered PS template was assembled via a centrifugation method reported previously.[1] About 45 mL of PS colloidal dispersions was ultrasonicated to form a uniform emulsion and then centrifuged at a rate of 3000 rpm for 12 h. The obtained precipitations were then dried at 60 ˚C overnight to obtain the final 3D ordered PS templates.

Preparation of 3D ordered porous Cu_2O cuboctahedra (3DOP Cu_2O-CO). In a typical synthesis of 3DOP Cu_2O-CO, monolithic 3D ordered PS template (about 4.0 g) was immersed into 40 mL aqueous solution containing 0.7 g of PVP and 2.0 g of $CuCl_2 \cdot 2H_2O$, 20 mL of ethanol and 20 mL of DI water for 12 h. The monolithic 3D ordered PS template filled with Cu^{2+} (denoted as PS@Cu^{2+} monolith) was taken out and treated under vacuum for 1 h to full fill the PS template interstices with Cu^{2+}. After drying at 60 ˚C for 5 h, the PS@Cu^{2+} monolith was put into an oven, where a small vessel containing 5.0 mL of ammonia was placed to evaporate ammonia vapor. After reacting for 12 h, the Cu^{2+} ions adsorbed in PS monolith were converted to $[Cu(NH_3)_n]^{2+}$ compound and the resultant monolith was denoted as PS@$[Cu(NH_3)_n]^{2+}$ monolith. After drying and evaporating excess ammonia at 50 ˚C overnight, 1.0 g of PS@$[Cu(NH_3)_n]^{2+}$ monolith was dropped into a 50 mL flask containing 0.7 g of PVP and 20 mL of DI water. After stirring for 1 h, 3.0 mL of 2.0 M NaOH solution was added and treated by vacuum degassing for 30 min. Finally, 2.0 mL of 0.5 M ascorbic acid solution was dropped into above solution with successively vacuum degassing for 10 min and reacting at 50 ˚C for 3 h. After completing the reaction, the PS templates were removed by dimethyl formamide (DMF). The precipitates were collected by washing/centrifugation cycles with ethanol. The 3DOP Cu_2O-CO powder was collected after drying the washed precipitates at 60 ˚C for 6 h.

Preparation of Cu_2O cuboctahedra (Cu_2O-CO). The Cu_2O-CO with equal size to that of 3DOP Cu_2O-CO was synthesized according to previous literature with some modifications.[2] In a typical preparation, 0.25 g of $CuCl_2 \cdot 2H_2O$ and 1.0 g of PVP were dissolved in 125 mL of DI-water under magnetic stirring. Then, 10 mL aqueous solution containing 0.75 g of NaOH was added to the above solution. After reacting for 5 min, 5.0 mL of glucose

solution (containing 0.75 g of glucose) was added. Then, the mixed solution kept reacting at 60 ˚C for 1.0 h. Finally, the products were collected by washing/centrifugation cycles with ethanol and drying at 60 ˚C.

Characterization: Scanning electron microscope (SEM) images were obtained using a Field emission scanning electron microscope (Zeiss Supra55) with an accelerating voltage of 10 kV. Transmission electron microscopy (TEM) and high-angle annular dark-field scanning TEM (HAADF-STEM) images were taken using a Talos F200X G2 microscope at an accelerating voltage of 200 kV. Wide-angle powder X-ray diffraction (XRD) profiles were recorded with a Bruker D8 Advance diffractometer with Cu-Kα radiation (λ = 1.54178 Å). X-ray photoelectron spectroscopy (XPS) was performed by PHI 5000 VersaProbe III with a monochromatic Al Kα X-ray source with the beam size of 200 μm. Charge compensation was achieved by dual beam charge neutralization and the binding energy was corrected by setting the binding energy of the hydrocarbon C 1s feature to 284.8 eV. Infrared spectra were recorded on a Nicolet iS10 FT-IR spectrometer on KBr pellets with wavenumbers ranging from 400 to 4000 cm^{-1}. The N_2 adsorption/desorption isotherms were measured by a Autosorb iQ (Quantachrome) instrument at 77 K. X-ray absorption spectroscopy (XAS) data of different samples K-edge were collected at BL14W1 beamline in Shanghai Synchrotron Radiation Facility (SSRF) in transmission mode, using a Si (311) double-crystal monochromator. The storage ring of SSRF was operated at 3.5 GeV with a maximum current of 240 mA. Cu foil was measured for energy calibration. CO_2 adsorption isotherms were measured by a Quantachrome Instrument ASiQMVH002-5 analyzer at 298K.

***In situ* attenuated total reflectance-surface enhanced infrared absorption spectroscopy (ATR-SEIRAS)**. ATR-SEIRAS were measured using a Thermo Scientific Nicolet iS50 FTIR Spectrometer with a Pike VeeMAX III attachment. 5 mg of the catalyst was dispersed in a mixture containing 0.96 mL of 2-propanol and 40 μL of 5 wt.% Nafion solution (Sigma-Aldrich). After being sonicated for 1 h, 100 μL of the suspension liquid was uniformly dropped onto the Au film. Spectra consisted of 64 scans at a spectral resolution of 4 cm^{-1} in a CO_2-saturated 0.1 M $KHCO_3$ electrolyte.

***In situ* Raman spectroscopy.** In situ Raman measurements were carried out using on a Jobin Yvon (Laboratory RAM HR800) confocal micro-Raman spectrometer through a long lens 50 × (NA=0.35) microscope objective with focal length about 18 mm. The laser light sources were an internal He-Ne laser with wavelength of 632.8 nm (16 mW). The Ag/AgCl, Pt gauze and catalyst electrode were employed as the reference, counter and working electrodes, respectively. The Raman spectra were recorded at different applied potential from 0 V to -0.5 V.

Finite-element method (FEM) Simulations. The 2D model was numerically simulated using the FLUENT software and combined with user-defined functions (UDFs) for CO_2RR in a porous medium reactor to simulate the species mass transport around individual catalyst particle.[3] The models of 3DOP Cu_2O-CO and Cu_2O-CO were established firstly, and a 2×2 μm^2 square was adopted. Three chemical species, CO_2, C_1 and C_2, each in a bulk and a surface adsorbed form, were defined to represent the CO_2 feedstock, the C_1 intermediate and product, the C_2 intermediate and product, respectively. Seven reactions were defined: four surface adsorption−desorption equilibrium reactions for the three chemical species as well as three irreversible reactions for the CO_2 reduction into C_1 and the C_1−C_1 dimerization into C_2. The species' diffusion coefficient, as well as the chemical dissociation reaction equations of CO_2 (aq.), C_1 (CO assumed) and C_2 (C_2H_4 assumed) were found in previous literatures.[4] The conductivity of the 3DOP Cu_2O-CO (Cu_2O) and the electrolyte (0.1 M $KHCO_3$) was taken from literature.[5]

Methods to construct HCO_3^-/CO_3^{2-} ratios *via* Raman spectra and pH calculations. For two Raman active species HCO_3^- and CO_3^{2-} in liquid phase, the relative concentrations are related to their Raman signal areas (*S*).

Origin 2021 was used to integrate signal areas. The $[HCO_3^-]/[CO_3^{2-}]$ is related to their Raman signal areas and the total carbon concentration is conserved, therefore, the $[HCO_3^-]$ and $[CO_3^{2-}]$ can be determined. Finally, pH values were calculated by the following equations through the pH-dependent equilibrium of HCO_3^-/CO_3^{2-}. The calculation was done with the CurTiPot pH analysis and simulation software version 4.3.1.

$$[H^+] = Ka \times \frac{[CO_3{}^{2-}]}{[HCO_3^-]}$$

$$\log \gamma = -AZ_i^2\left(\frac{\sqrt{I}}{1+\sqrt{I}} - 0.2I\right)$$

$$pH = -\log H^+ = -\log\left([H^+] \times \gamma H^+\right)$$

Where *K*a is the dissociation constant of carbonic acid, *A* is constant, Z_i is the valence of ion, *I* is the ionic strength of the solution, $[H^+]$ and γH^+ represent the proton concentration and proton activity coefficient, respectively.

Electrochemical Measurement. The catalyst modified glassy carbon electrode (GCE) was firstly made according to the following procedure: 2 mg of catalyst (3DOP Cu_2O-CO, 3DOP-Cu_2O-SPs, Cu_2O-CO or Cu_2O-SPs powder) and 8 mg of Vulcan XC-72 carbon were dispersed in a mixed solution containing 800 μL of isopropanol, 100 μL of H_2O and 100 μL of Nafion solution (5%). The mixture was sonicated for 1 h to form a homogeneous catalyst ink. Then, 10 μL of the catalyst ink was deposited on the surface of GCE (diameter of 5 mm). In avoid of influences of adsorbates or catalyst changes, the GCE was mechanically polished with alumina paste, followed by sonication in DI-water and blow by nitrogen gas before catalyst coating. After drying the catalyst ink in atmospheric condition, the catalyst-modified GCE was directly used as working electrode.

Electrochemical CO_2RR in H-type cell. Electrochemical studies were carried out in a custom-made two-compartment H-type cell, in which the working and counter electrodes were separated by a 117 Nafion® membrane. Each compartment of the cell was filled with 30 mL of 0.1 M $KHCO_3$. All the electrochemical signals were recorded by using an electrochemical workstation (PARSTAT 3000A, Princeton Applied Research). Before and during the electrochemical reaction, the electrolyte was purged continuously with CO_2 (20 mL min^{-1}) from the bottom of the cell under magnetic stirring. The gas flow was regulated using a mass flow controller. The three-electrode configuration consists of Ag/AgCl as reference electrode, a platinum plate (1×1 cm^2) as counter electrode and catalyst-modified GCE as working electrode. Every measurement started with a linear sweep voltammetry (potential ranging from -0.4 V to -1.7 V, scan rate of 5 mV s^{-1}) and followed by a chronoamperometric step for one hour at various potentials. The electrochemical impedance spectroscopy (EIS) was performed at −1.0 V (vs. Ag/AgCl) under the same condition. The frequency limits were typically set in the range from 0.01 Hz to 100 kHz with a voltage amplitude of 10 mV. All of the applied potentials were recorded against an Ag/AgCl (saturated KCl) reference electrode and then converted to those versus reversible hydrogen electrode (RHE) by E (vs RHE) = E (vs Ag/AgCl) + 0.197 V + 0.0591*pH.

Electrochemical CO_2RR in Flow cell reactor. The flow cell electrolyzer (Aida Hengsheng Technology Development Co., Ltd.) equipped with a gas diffusion layer cathode, a reference electrode Ag/AgCl (saturated KCl), and a nickel foam anode was adopted. The cathode and anode chambers were separated by an anion exchange

membrane (AEM, FAA-3PK-130, Fumatech) with a flowing 1.0 M KOH solution as both the catholyte and the anolyte. The electrolyte at the cathode and anode was circulated by a peristaltic pump with a flow rate of 10 mL min^{-1}. CO_2 entered the cathode gas chamber at a constant rate (40 mL min^{-1}) and continuously diffused into the interior of the gas diffusion electrode for the CO_2RR. To fabricate the working electrode, a certain amount of catalysts (10 mg) were dispersed in 1mL of ethanol with 80 μL of 5 wt% Nafion solution. After mixing thoroughly under sonication, the catalyst ink was spray-coated onto a gas diffusion layer (GDL, YSL-30T) to obtain gas-diffusion electrode (GDE). The loading amount of catalyst on GDE was controlled to be 0.3 mg cm^{-2}. The working electrode was placed between gas and catholyte chambers to ensure gaseous CO_2 diffusion and reaction at the catholyte/catalysts interface. An electrochemical workstation (PARSTAT 3000A, Princeton Applied Research) with a current amplifier was used to perform the CO_2RR test. Reactions were tested via chronopotentiometry at differing currents for 1 h without iR correction.

Evaluation of CO_2RR performance. After the gas stream passed the CO_2R cell, it was directly introduced into a Gas Chromatograph (GC, Aglilent GC 8890). The gas flow rate was confirmed by using a mass flow controller installed between the gas outlet of H-type cell and gas inlet of GC. A Flame Ionization Detector (FID, for CO, CH_4, C_2H_4, C_2H_2, C_3H_6, C_3H_8 and C_4H_8) and a Thermal Conductivity Detector (TCD, for H_2) were used to quantify gaseous products.

The liquid products were sampled from the catholyte after reaction at constant potential by a syringe. For quantifying the liquid products, 0.5 mL of the collected electrolyte was mixed with 0.1 mL of D_2O (deuterated water) and 0.05 μL of dimethyl sulfoxide (DMSO, used as internal standard), and subsequently analyzed by ^{1}H nuclear magnetic resonance (^{1}H-NMR). The ^{1}H-NMR spectrum was measured with water suppression using a pre-saturation method.

After the quantification, the faradaic efficiency (FE) for the products were calculated as follows:

$$\text{FE (\%)} = \frac{e \times F \times n}{Q} \times 100\%$$

where, *e* is number of electrons transferred for different products, *Q* is the total charge, *n* is the total amount of different product (in moles), and F is the Faraday constant (96485 C mol^{-1}).

The formation rate (R) for each species was calculated using the following equation:

$$R = (q_{tot} \times FE) / (96485 \times z \times t \times S)$$

where, t is the electrolysis time (h) and S is the geometric area of the electrode (cm^2).

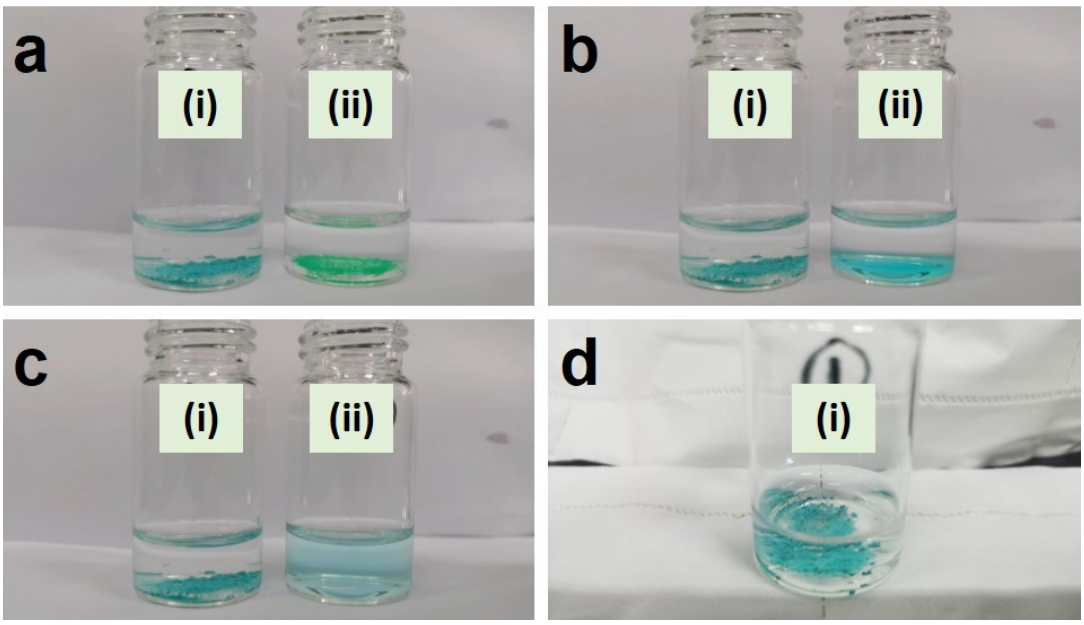

Figure S1 Photographs of the dissolution process of $[Cu(NH_3)_n]^{2+}$ (i) and $CuCl_2{\cdot}2H_2O$ (ii) after mixing with H_2O for different time periods: (a) 0 min, (b) 1 min, (c) 4 min and (d) 24 h, respectively.

Note: The $[Cu(NH_3)_n]^{2+}$ used in the dissolution comparison was obtained by exposing $CuCl_2{\cdot}2H_2O$ powder to the NH_3 vapor in an air-tight container.

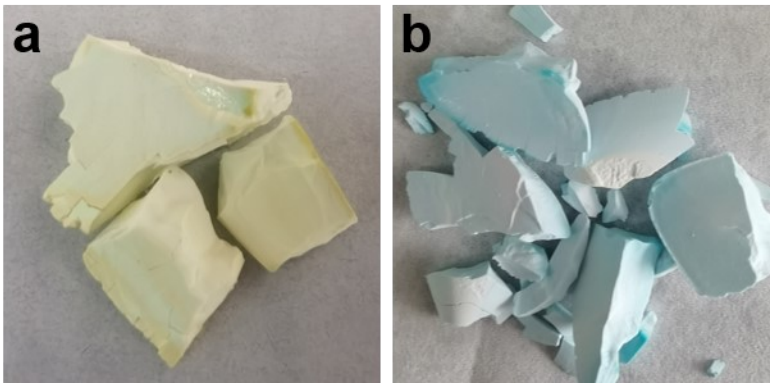

Figure S2 Photographs of PS cake filled with Cu^{2+} (a) before and (b) after ammonia treatment. Both photographs were taken after the drying treatment.

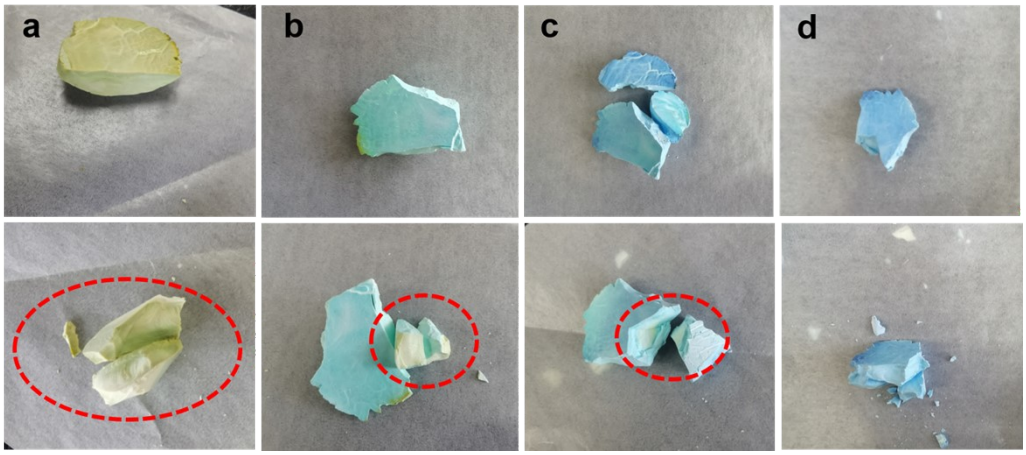

Figure S3 The photographs of PS@Cu^{2+} monoliths treated with saturated ammonia vapor for different time: (a) 1 min, (b) 10 min, (c) 30 min and (d) 60 min, respectively. Photographs in the top and bottom rows are used to show the color of exterior surface and fresh broken surface, respectively.

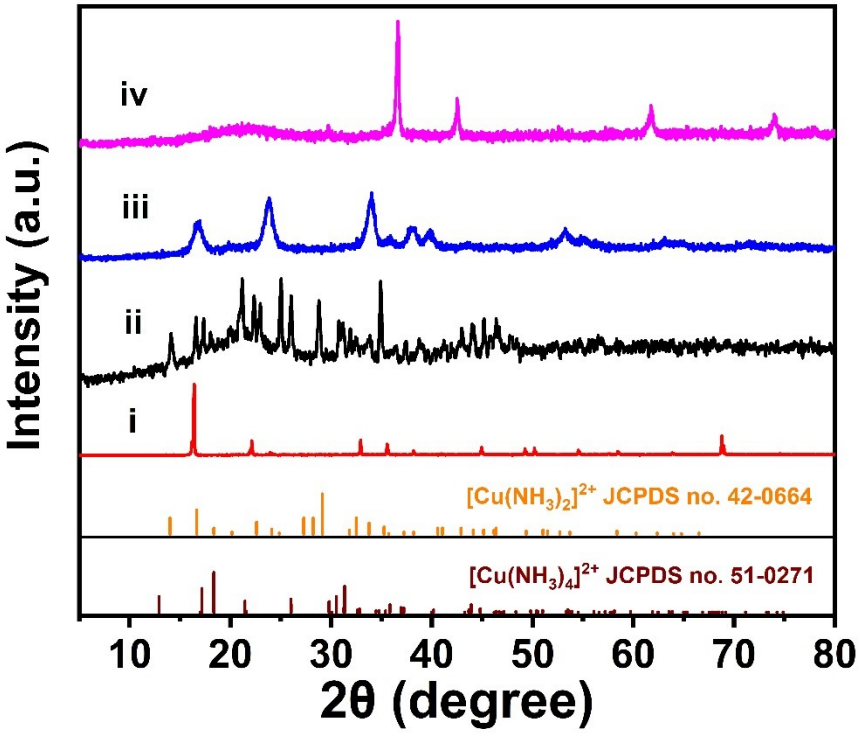

Figure S4 XRD patterns of (i) $CuCl_2 \cdot 2H_2O$ powder, (ii) Cu^{2+}-PS monolith after ammonia treatment, (iii) $Cu(OH)_2$ and (iv) Cu_2O. The standard diffraction patterns of $[Cu(NH_3)_2]^{2+}$ and $[Cu(NH_3)_4]^{2+}$ are shown for reference.

Note: The ammonia treatment was carried out in an air-tight container with saturated ammonia vapor. The $Cu(OH)_2$ was prepared by mixing 20 mL of 50 mM $CuCl_2$ and 2 mL of 2 M NaOH solution. Profile iv is the XRD pattern of as-prepared 3DOP Cu_2O-CO.

For making abundant sample for XRD measurement, only the cyan colored sample is scratched and collected after the PS@Cu^{2+} monolith was treated with ammonia. This operation was repeated till enough XRD sample was made.

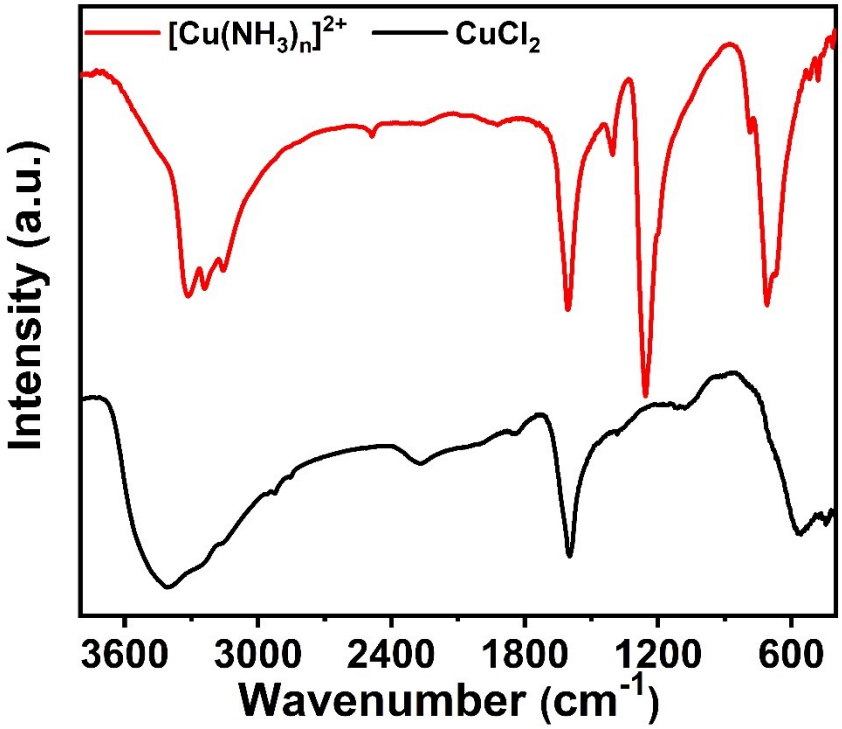

Figure S5 FTIR profiles of $[Cu(NH_3)_n]^{2+}$ and $CuCl_2$.

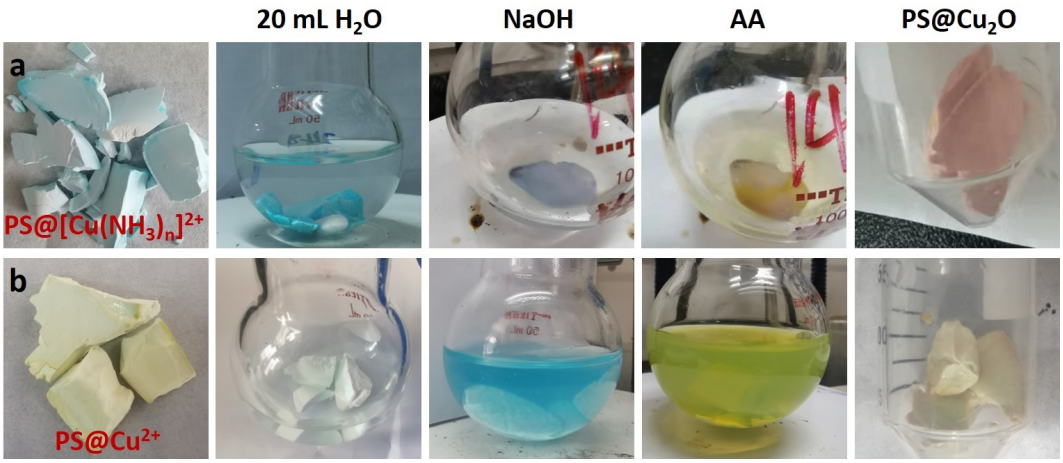

Figure S6 Photographs of different reaction stages to form porous Cu_2O by using (a) PS@$[Cu(NH_3)_n]^{2+}$ and (b) PS@Cu^{2+} as the precursor, respectively.

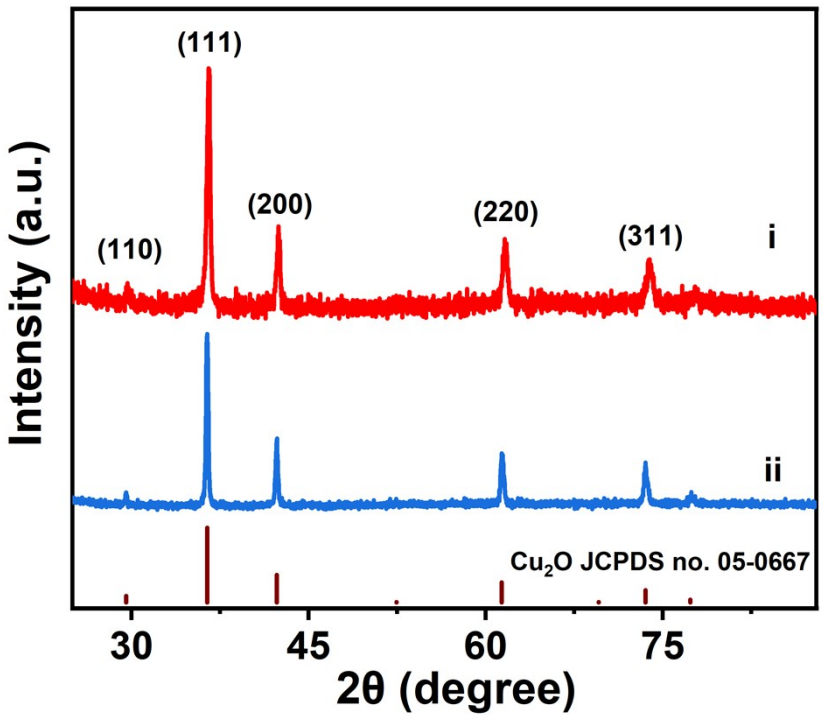

Figure S7 XRD patterns of (i) 3DOP Cu_2O-CO and (ii) Cu_2O-CO. The standard diffraction patterns of Cu_2O are shown for reference.

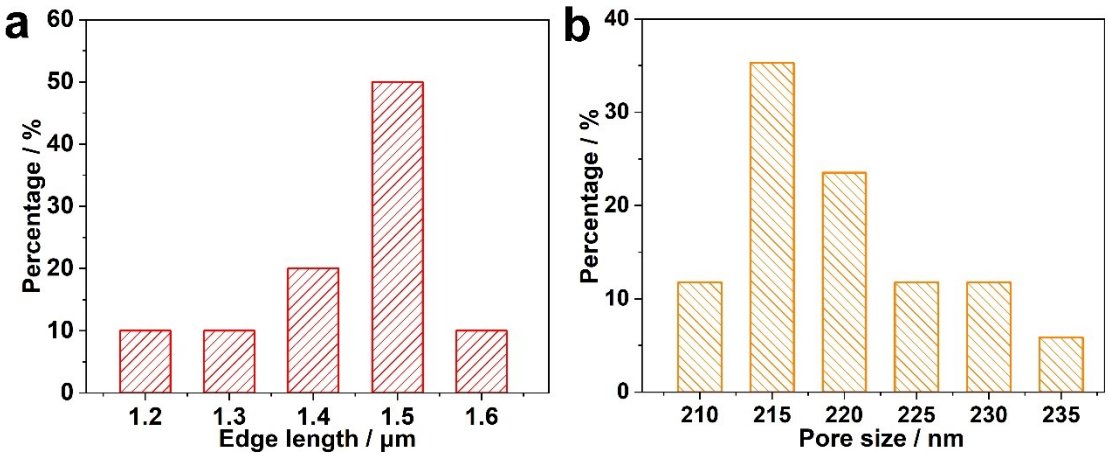

Figure S8 Histograms of the (a) edge length and (b) pore size distributions of the obtained 3DOP Cu_2O-CO.

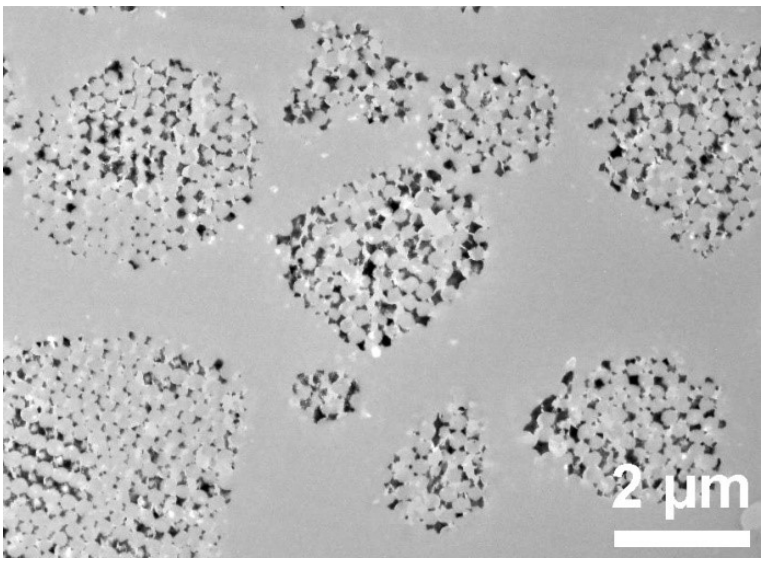

Figure S9 TEM image of the sliced sample revealing the pore connections inside the 3DOP Cu_2O-CO.

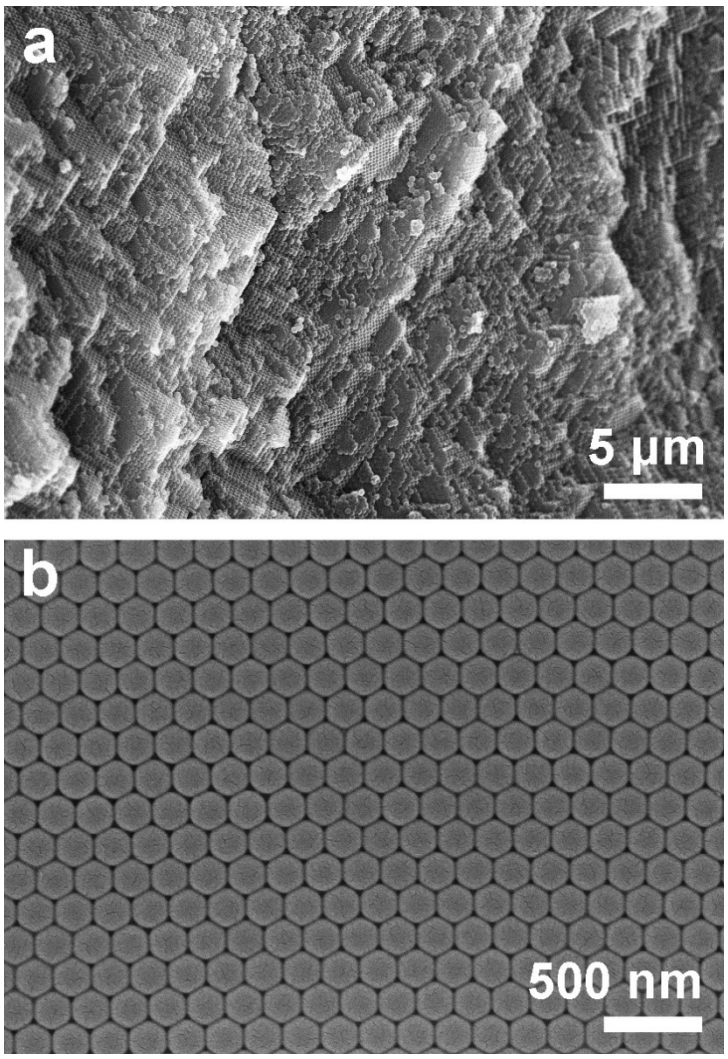

Figure S10 Typical SEM images of the assembled PS template.

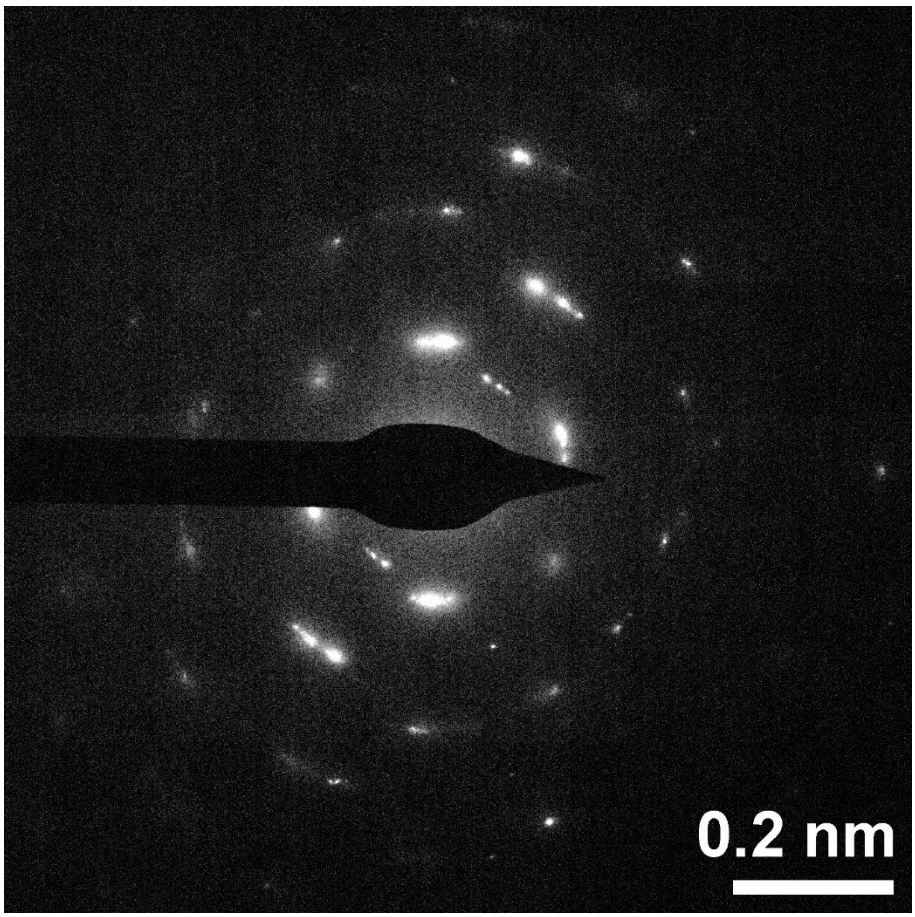

Figure S11 SAED pattern derived from one individual 3DOP Cu_2O-CO particle.

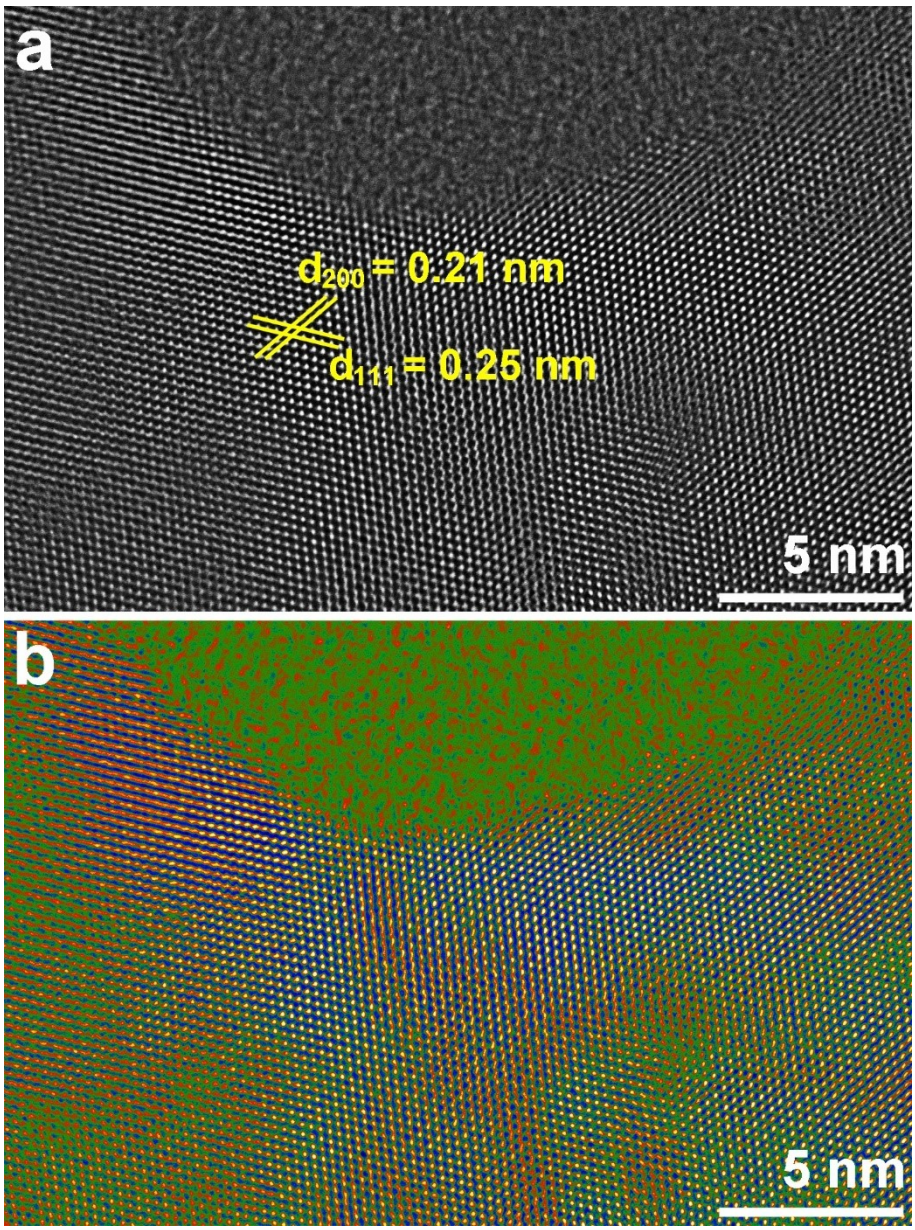

Figure S12 Aberration-corrected HAADF images of the concave surface of the 3DOP Cu_2O-CO.

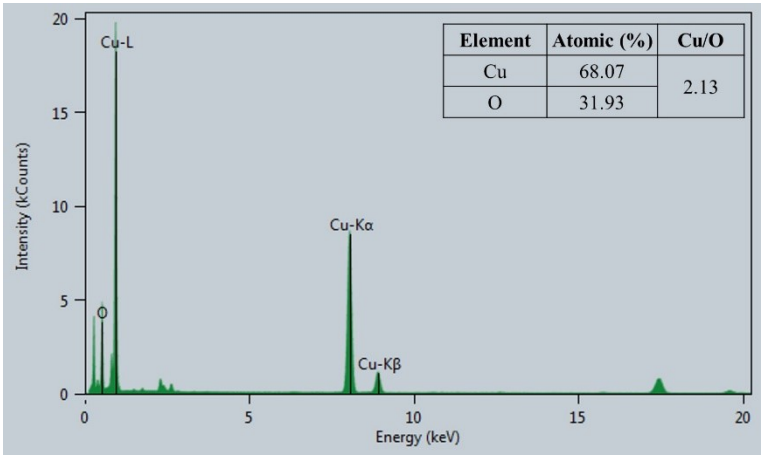

Figure S13 EDS results revealing the atomic ratio between Cu and O of the prepared 3DOP Cu_2O-CO.

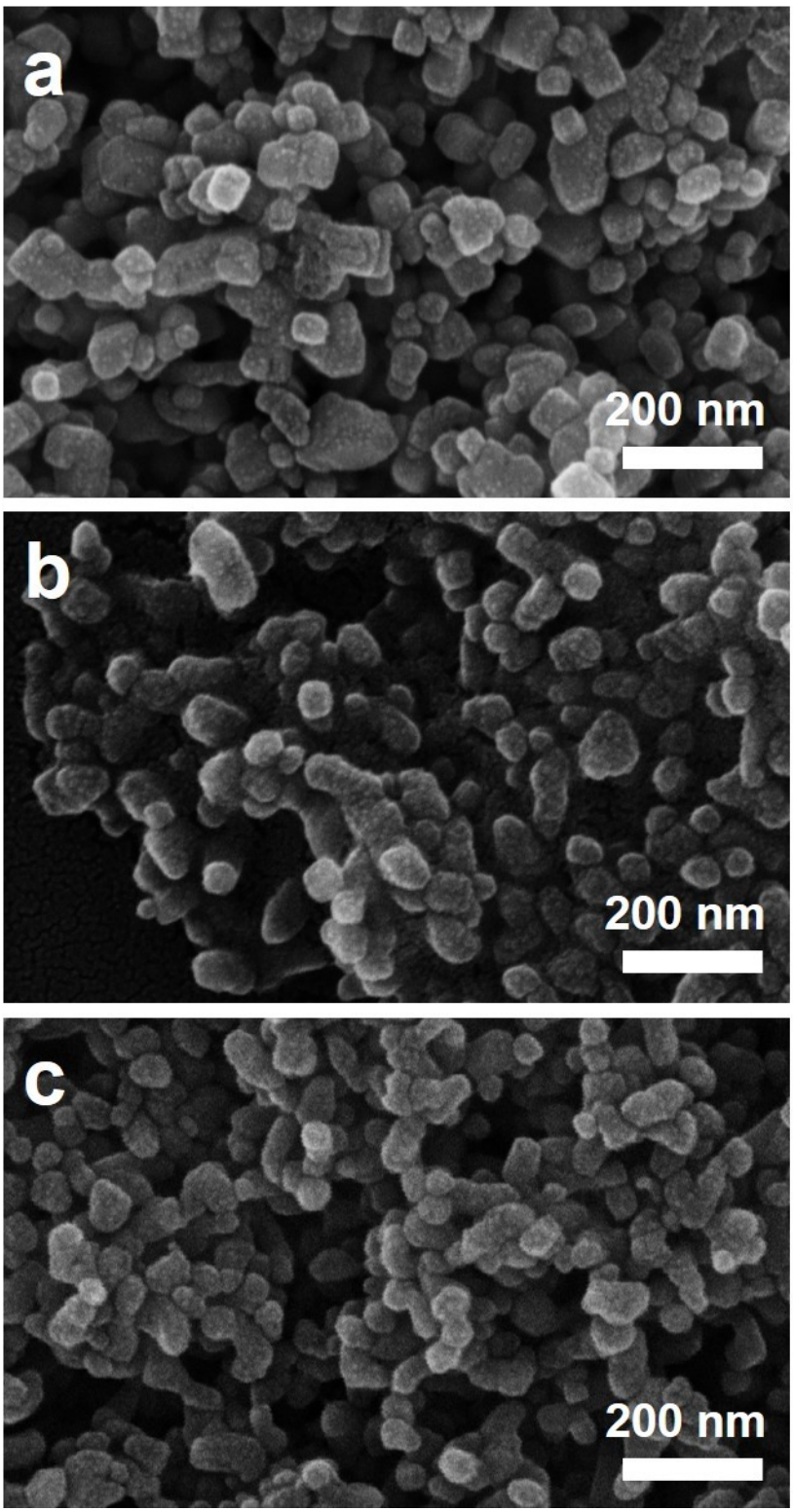

Figure S14 SEM images of the samples prepared under the same synthetic procedure to that of 3DOP Cu_2O-CO except without using PS template. To better reveal the PVP effect, three batches of synthesis were carried out by using different amount of PVP: (a) 0 g, (b) 0.35 g and (c) 0.70 g.

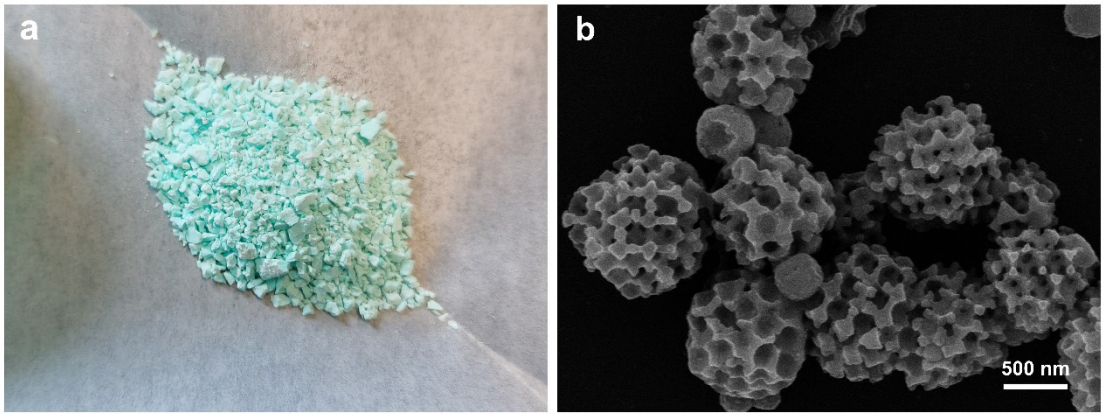

Figure S15 (a) Photograph of the powder template obtained by grinding PS@Cu$[(NH_3)_n]^{2+}$ monolith. (b) The products obtained under the same condition to that of 3DOP Cu_2O-CO except using the powder template shown in panel (a) instead of monolith template.

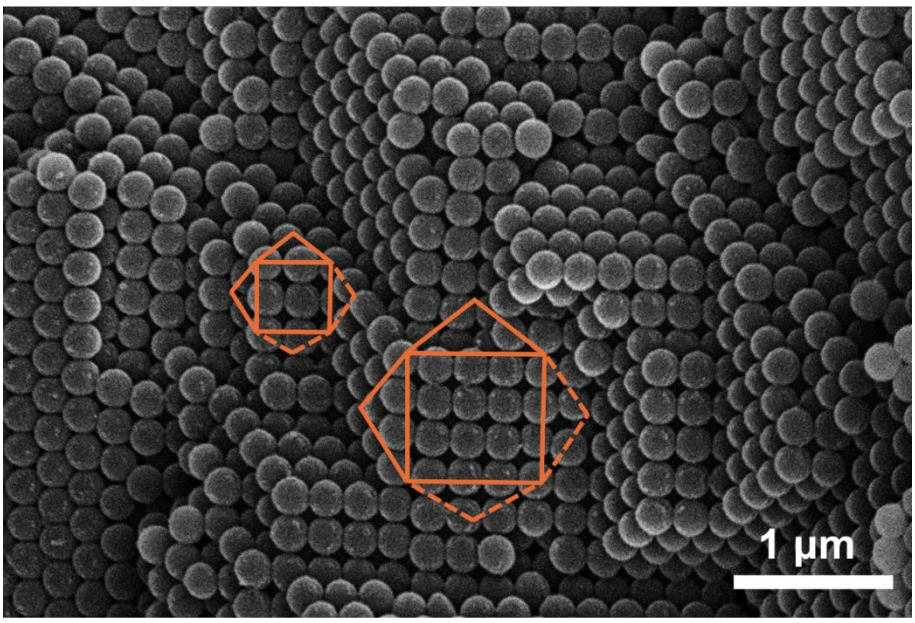

Figure S16 Cross-sectional SEM image of the assembled PS spheres to reveal the assembled manner of PS spheres.

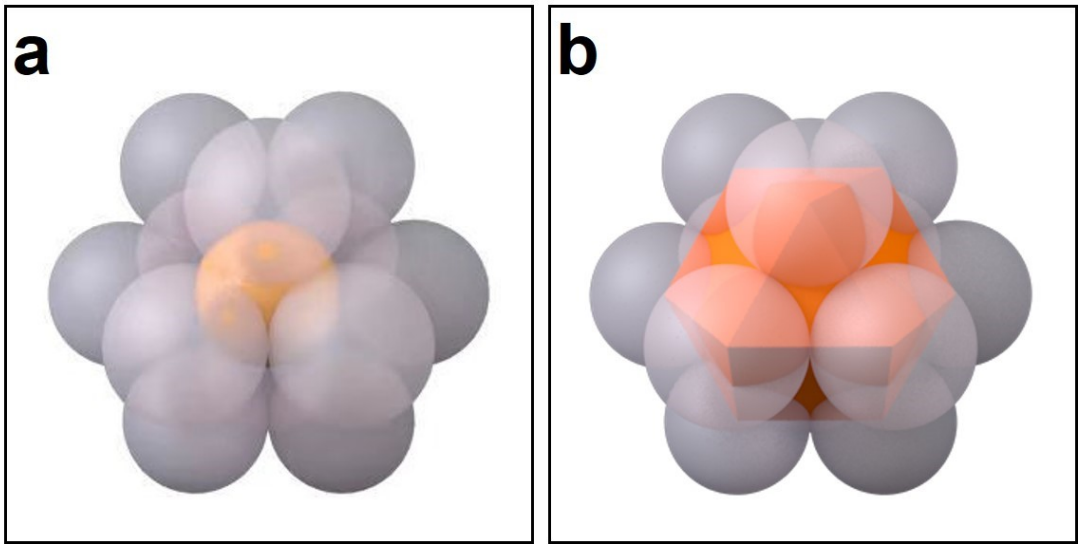

Figure S17 Schematic illustration of (a) a close-packed unit cell and (b) the geometric relationship between a cuboctahedron and close-packed unit cell.

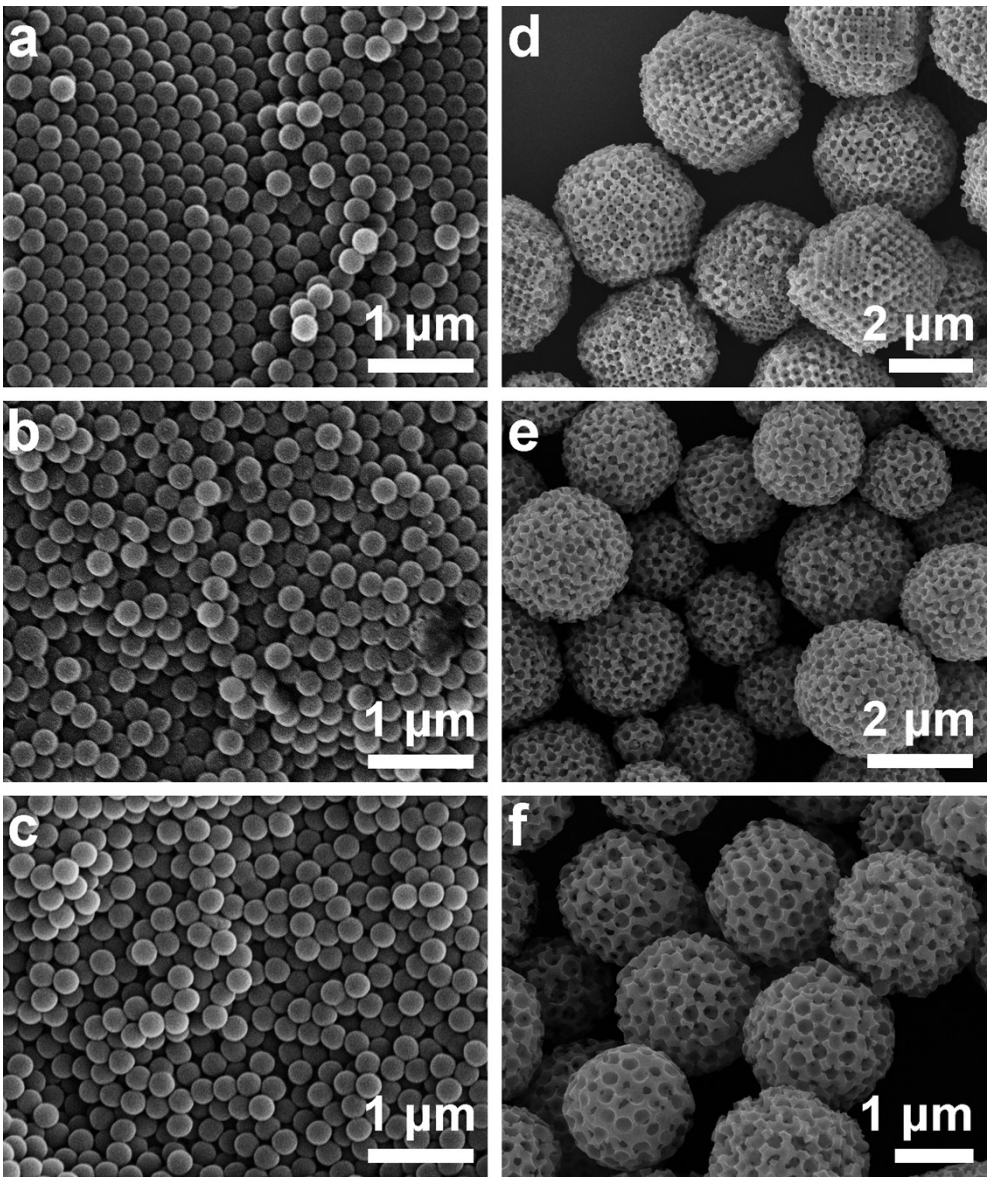

Figure S18 (a-c) Typical SEM images of the assembled PS template by using the solvent evaporation method under different temperatures: (a) 30 ˚C, (b) 40 ˚C and (c) 50 ˚C. (d-f) Typical SEM images of the obtained products by using the assembled PS template shown on the left side.

Note: With increasing temperature from 30 ˚C to 40 ˚C and 50 ˚C, the assembled PS template changed from ordered assembly, to partially ordered assembly and disordered assembly.

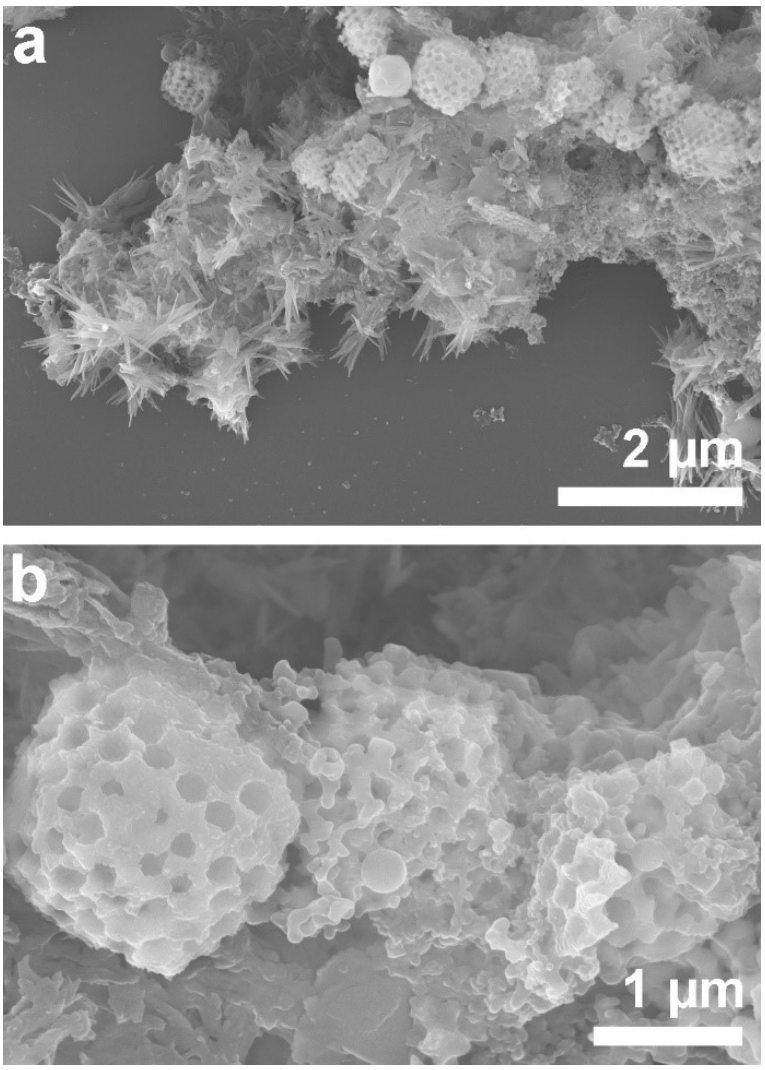

Figure S19 Typical SEM images of the products synthesized with the same condition to that of 3DOP Cu_2O-CO but without ammonia treatment.

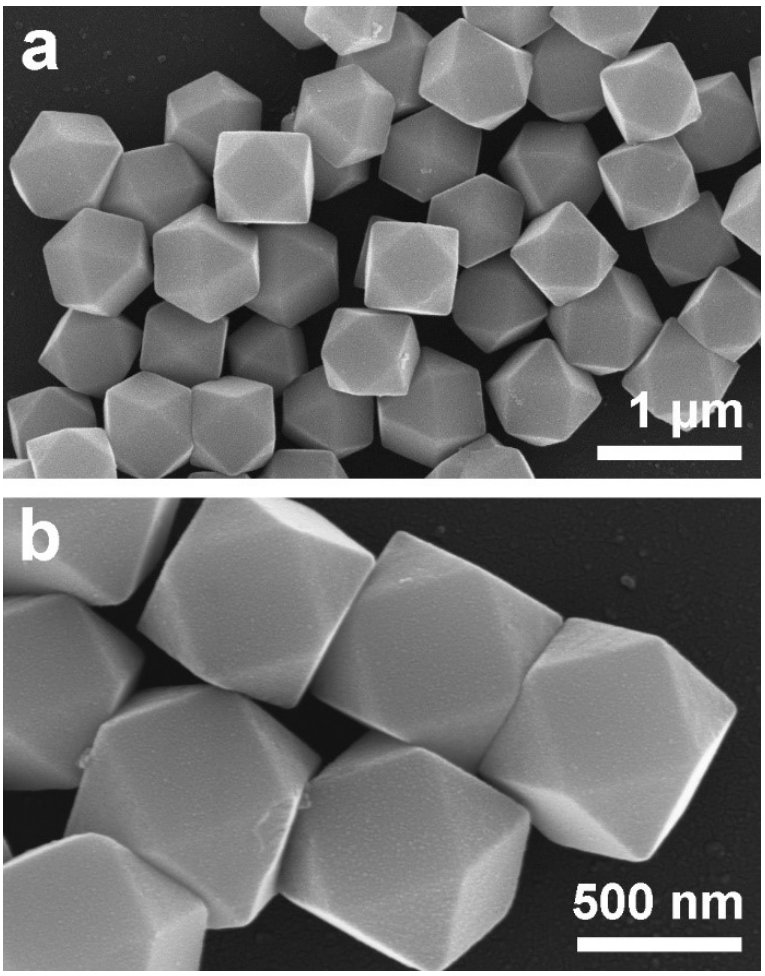

Figure S20 Typical SEM images of the Cu_2O-CO with (a) low and (b) high magnifications.

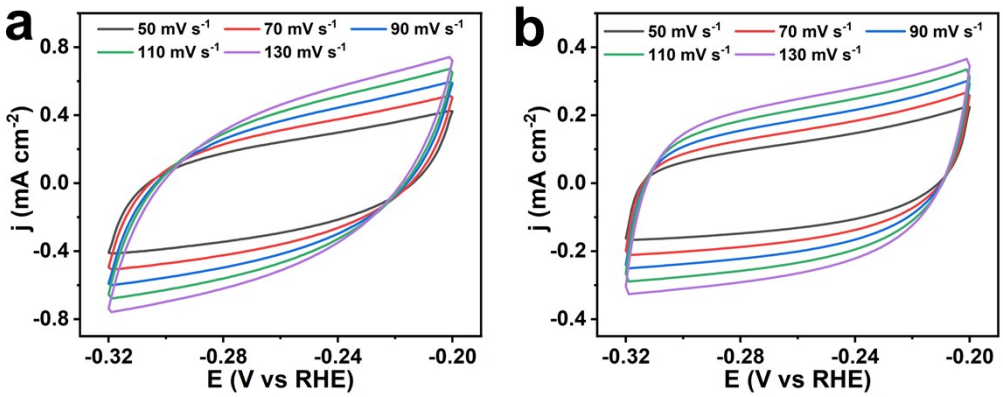

Figure S21 CV curves at a potential range of 0.28-0.4 V in N_2-saturated 0.1 M $KHCO_3$ solution for (a) 3DOP Cu_2O-CO and (b) Cu_2O-CO.

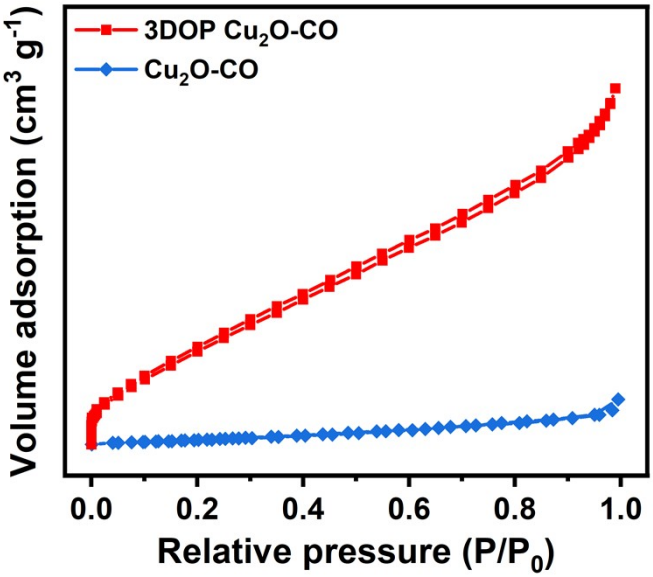

Figure S22 N_2 adsorption-desorption isotherms of 3DOP Cu_2O-CO and Cu_2O-CO.

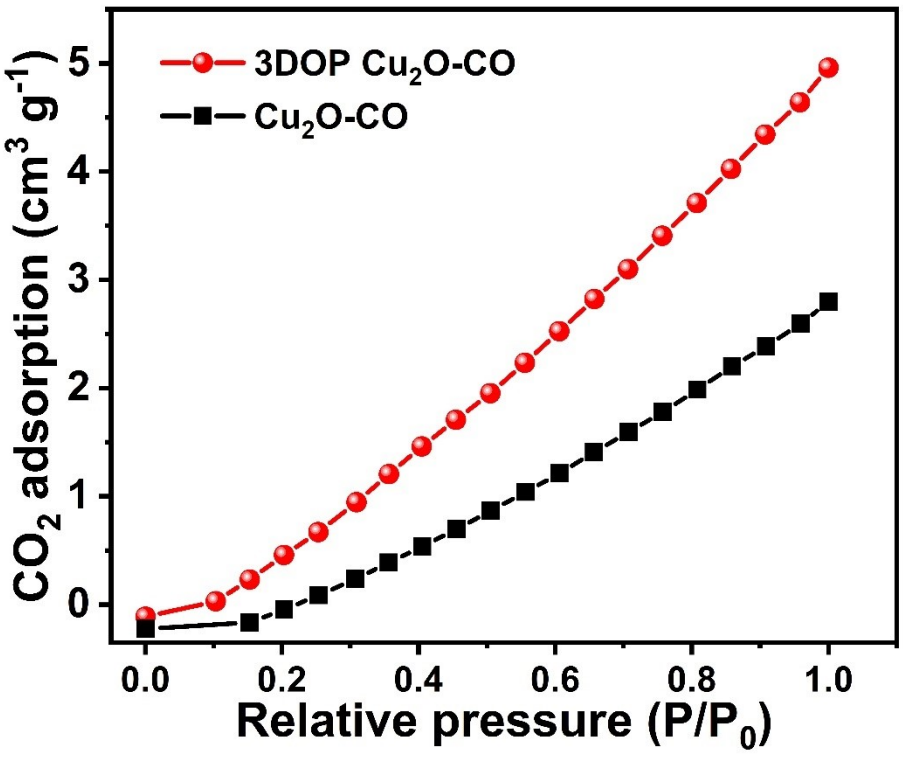

Figure S23 Carbon dioxide adsorption isotherms at 25 ˚C for 3DOP Cu_2O-CO and Cu_2O-CO, respectively.

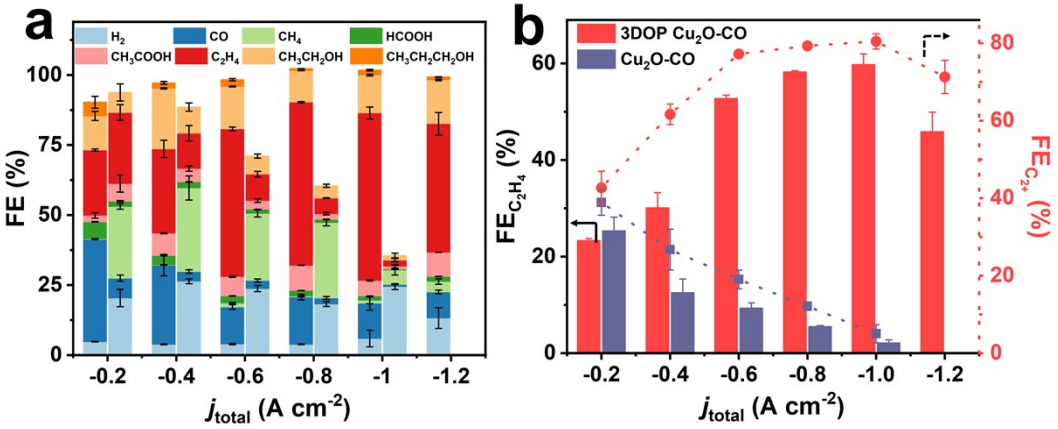

Figure S24 (a) FE of the products and (b) C_2H_4 and C_{2+} FEs at various applied potentials for 3DOP Cu_2O-CO (left-side histogram) and Cu_2O-CO (right-side histogram), respectively.

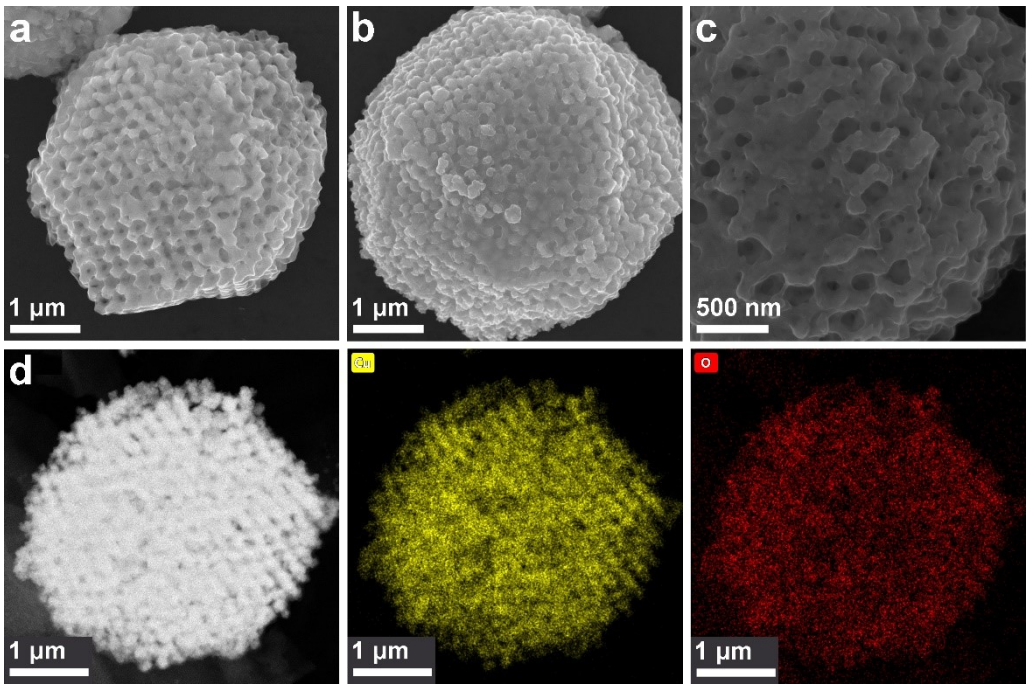

Figure S25 Typical SEM images of the 3DOP Cu_2O-CO after electrocatalyzing CO_2RR for 24 h.

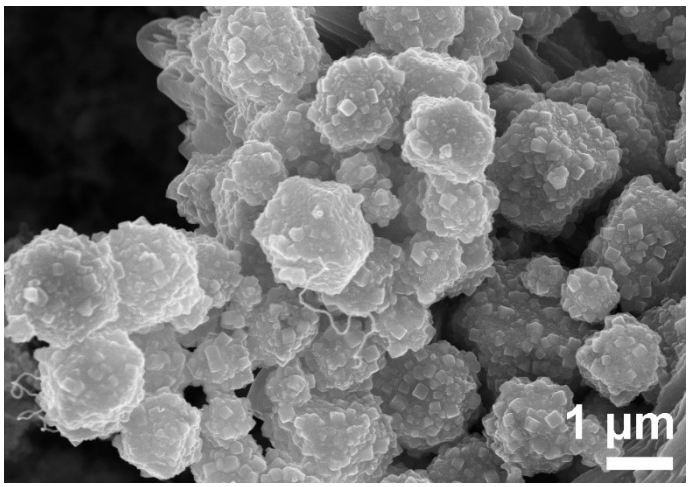

Figure S26 Typical SEM image of the Cu_2O-CO after electrocatalyzing CO_2R for 24 h.

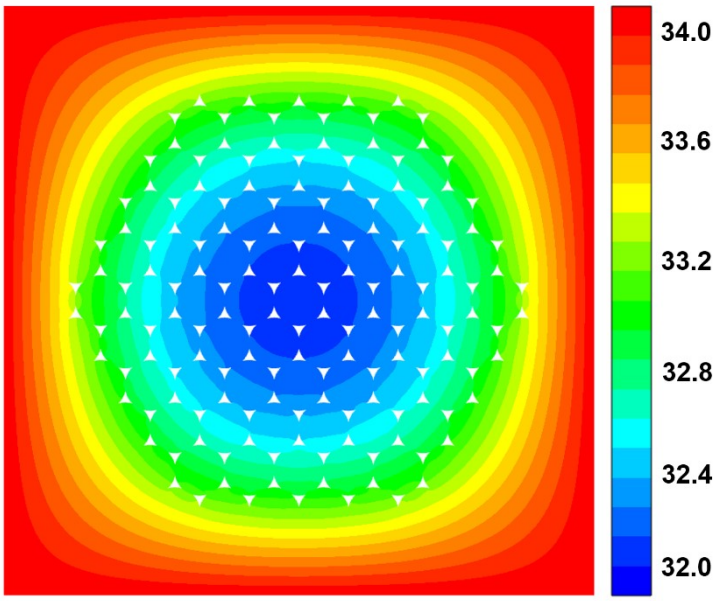

Figure S27 Finite-element method simulation of CO_2 distribution over 3DOP Cu_2O-CO.

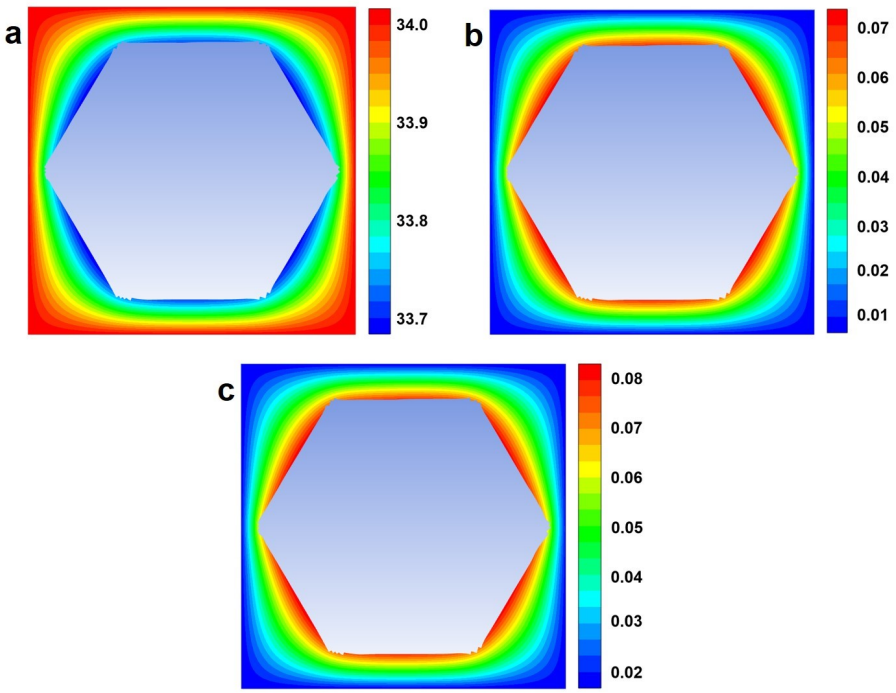

Figure S28 The FEM simulated distributions of (a) CO_2, (b) C_1 and (c) C_2 over Cu_2O-CO.

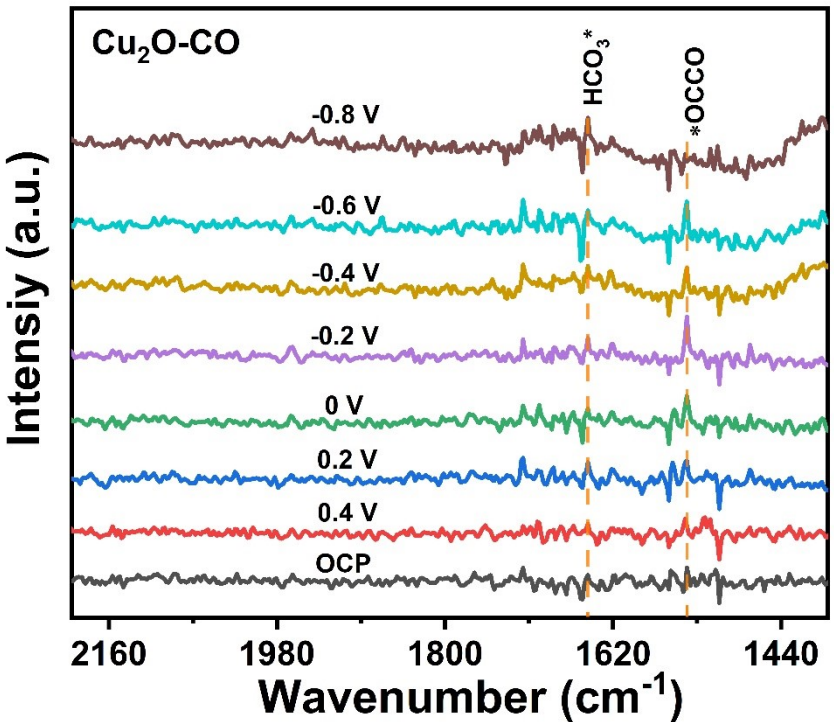

Figure S29 *In situ* ATR-SEIRAS spectra of Cu_2O-CO from OCP to -0.8 V vs. RHE in CO_2-saturated 0.1 M $KHCO_3$ aqueous solution.

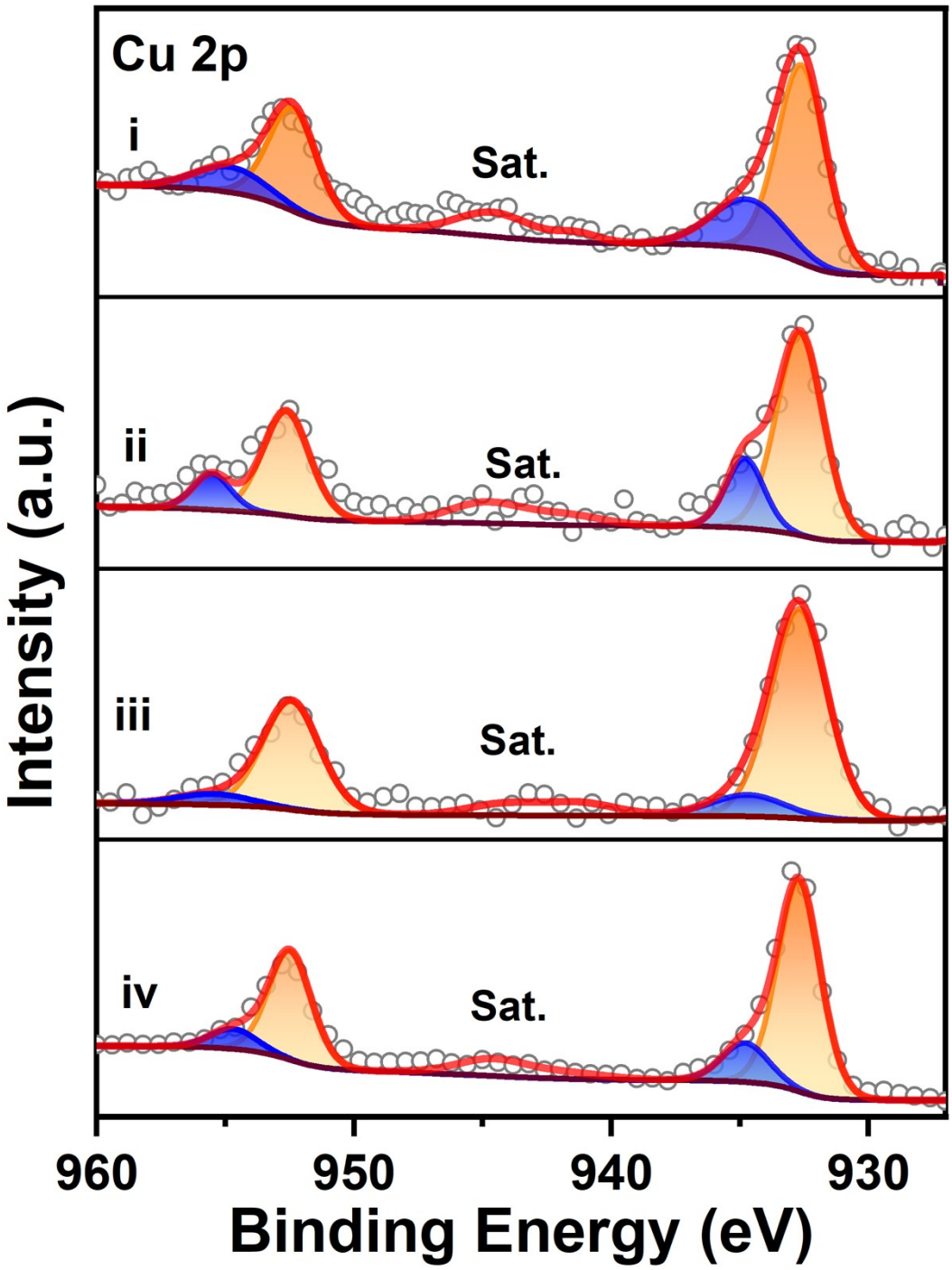

Figure S30 XPS spectra of Cu 2*p* for (i) 3DOP Cu_2O-CO, (ii) Cu_2O-CO, (iii) 3DOP Cu_2O-CO-A and (iv) Cu_2O-CO-A. The compositions of the fitted plots are Cu_2O (orange plot), CuO (blue plot and satellite peak) and Cu (green plot). 3DOP Cu_2O-CO-A and Cu_2O-CO-A represent the corresponding samples after electrocatalyzing CO_2 for 5 h.

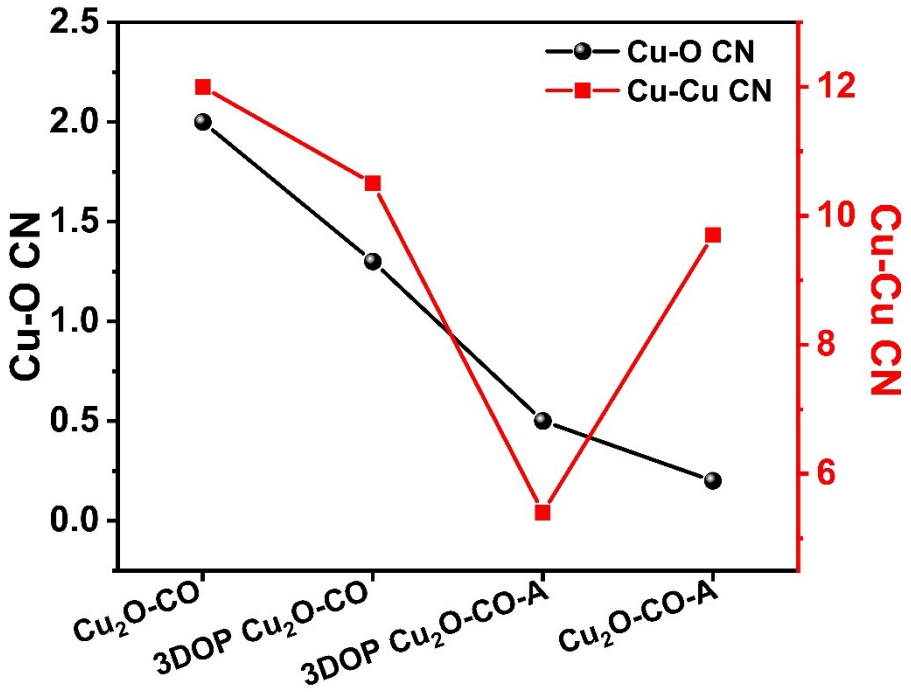

Figure S31 The Cu-O CN and Cu-Cu CN for 3DOP Cu_2O-CO, 3DOP Cu_2O-CO after electrocatalyzing CO_2 (3DOP Cu_2O-CO-A), Cu_2O-CO and Cu_2O-CO after electrocatalyzing CO_2 (CO_2-CO-A), respectively.

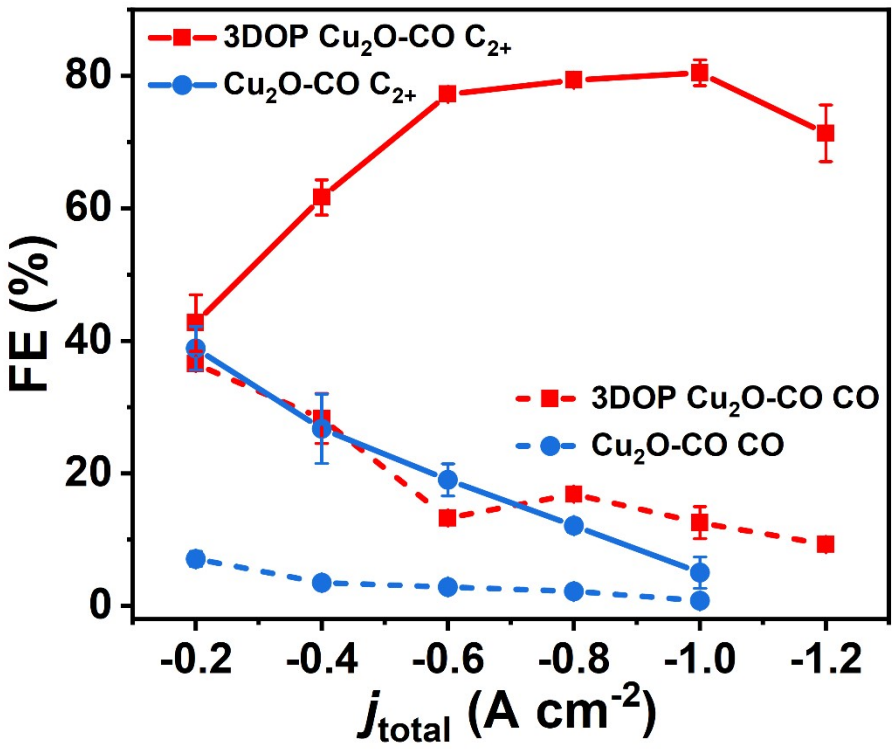

Figure S32 FEs for C_{2+} and CO products over 3DOP Cu_2O-CO and Cu_2O-CO samples.

Table S1 The grain size of different samples calculated by using the Scherrer equation based on the most intense (111) diffraction peak.

Samples	Grain size (nm)
3DOP Cu_2O-CO	23.6
Cu_2O-CO	43.4

Table S2 Product analysis of electrochemical CO_2RR at different potentials for the as-prepared samples in H-type cell and flow cell reactor, respectively.

	E (V vs	FE_{H2} (%)	FE_{CO} (%)	FE_{CH4} (%)	FE_{HCOOH} (%)	$FE_{CH3COOH}$	FE_{C2H4} (%)	FE_{C2H5OH} (%)	FE_{C3H7OH} (%)
H-Cell									
3DOP Cu_2O-CO	-1.2	18.2	7.6	0.0	15.3	0.0	30.2	10.5	5.9
	-1.3	17.7	5.8	1.9	13.3	0.0	42.6	7.7	6.9
	-1.4	13.4	2.9	2.9	8.0	2.0	51.3	13.0	7.1
	-1.5	12.6	2.7	2.5	9.8	0.9	46.0	11.2	7.4
	-1.6	14.9	1.6	4.0	5.2	0.8	48.6	11.3	4.4
	-1.7	24.0	1.0	5.9	2.9	0.9	37.4	10.1	3.6
Cu_2O-CO	-1.2	27.4	4.1	5.9	16.9	0.4	30.6	8.2	0.9
	-1.3	11.0	1.9	10.3	8.0	0.0	37.2	7.4	6.5
	-1.4	14.0	0.9	14.9	4.3	0.8	37.9	14.8	2.8
	-1.5	11.7	0.7	14.1	2.9	1.5	37.1	15.2	0.0
	-1.6	23.3	0.4	17.6	2.3	1.4	20.5	9.2	4.5
	-1.7	43.4	0.5	20.6	1.8	0.7	15.5	1.4	0.6
Flow Cell									
3DOP Cu_2O-CO	-200	4.7	25.3	0.6	6.2	3.0	23.1	13.3	6.4
	-400	3.7	31.0	0.2	3.4	8.1	28.0	21.6	2.4
	-600	5.0	13.5	0.7	2.6	7.1	52.3	15.3	2.7
	-800	3.8	17.6	0.2	2.3	9.8	58.2	12.2	0.8
	-1000	3.7	14.1	0.3	1.7	6.0	61.3	14.9	1.8
	-1200	10.7	9.8	3.0	1.8	8.7	48.7	15.2	1.1
Cu_2O-CO	-200	36.0	19.3	11.4	3.1	2.5	21.2	8.8	0.0
	-400	21.5	14.6	9.2	3.3	5.2	19.3	11.8	0.3
	-600	20.0	10.6	14.6	2.3	5.3	23.8	10.9	0.3
	-800	19.5	6.4	18.9	4.2	9.0	17.2	14.7	0.3
	-1000	20.8	6.6	17.6	3.5	9.1	15.8	13.1	1.1

Table S3 Comparison of current densities and FEs towards specific products of 3DOP Cu_2O-CO with previously reported Cu-based electrocatalysts

Catalyst	System	E (V vs. RHE)	FE_{C2H4} (%)	j_{C2H4} (mA cm^{-2})	FE_{C2} (%)	j_{C2} (mA cm^2)	References
Cu nanocube	H cell	-1.0	45.0	21.5	73	35.0	6
Cu_2O NPs	H cell	1.1	59	22.0	59	22.0	7
Cu-on-Cu_3N	H cell	-1.35	39	25	64	41	8
o-Cu_2O	H cell	-1.1	18	6.6	48.3	17.7	9
18-nm Cu_2O	H cell	-0.98	43	13.3	60	18.7	10
CuO_x Nanocubes	H cell	-0.97	34	1.9	48	2.6	11
Cu_2O derived copper	Flow cell	/	40	120	74.9	225	12
3-shell HoMSs Cu_2O	Flow cell	/	32	214	77	514	13
Multi-hollow Cu_2O	Flow cell	/	40	142	75.2	267	14
$Cu_xO_yC_z$	Flow cell	/	34	50.3	54	80	15
Electro-redeposited Cu	Flow cell	/	38	113	54	161	16
Ag@Cu	Flow cell	/	15	48	50	160	17
B-Cu_2O	Flow cell	/	50	192.8	77.8	300	18
CuO_x	Flow cell	/	34	102	60	180	11
$Cu_2P_2O_7$	Flow cell	/	39	185.5	73.6	350	19
Hierarchical Cu	Flow cell	/	31.8	127	64.0	255	20
Cu-CuI	Flow cell	/	34.0	283	71.0	591	21
Cu_3-Br	Flow cell	/	55	330	55.0	330	22
(100)-Orientaoted CuO	Flow cell	/	32	224	58.6	410	23
N-Cu	Flow cell	/	51	629	73.7	909	24
Nanoporous Cu	Flow cell	/	**38.6**	256	62	411	25
3DOP Cu_2O-CO	H cell	**-1.0**	**51.3**	**9.2**	**73.4**	**13.2**	**This work**
3DOP Cu_2O-CO	Flow cell	/	**61.3**	**613**	**81.7**	**817**	**This work**

Table S4 the CO_3^{2-}/HCO_3^- ratio of 3DOP Cu_2O-CO and Cu_2O-CO in Raman spectra.

E (V vs RHE)	3DOP Cu_2O-CO	Cu_2O-CO
0	9.8	3.2
-0.1	15.7	4.0
-0.2	20.8	7.1
-0.3	26.9	7.5
-0.4	30.7	2.0
-0.5	35.8	4.1

Table S5 Fitting parameters and peak for the fitting model of the Cu 2*p* deconvolution shown in Figure 6a. The peak fitting was carried out based on previous report. [26]

Peaks	Position (eV)	ΔPosition (eV)	Attribution
Cu^0 2*p*	932.66		Cu^0 $2p_{3/2}$
	952.64	19.98	Cu^0 $2p_{1/2}$
Cu^{2+} 2*p*	934.80		Cu^{2+} $2p_{3/2}$
	955.54	20.74	Cu^{2+} $2p_{1/2}$

Table S6 The composition analysis of different samples before and after electrocatalyzing CO_2RR for 5 h. The analysis is derived from Figure 6b. The peak fitting was carried out based on previous report.[27]

Samples	Cu^0 (%)	Cu^+ (%)	Cu^{2+} (%)
3DOP Cu_2O-CO	0	82	18
Cu_2O-CO	0	69	31
3DOP Cu_2O-CO-A	35	54	11
Cu_2O-CO-A	36	42	22

Note: 3DOP Cu_2O-CO-A and Cu_2O-CO-A represent the corresponding samples after electrocatalyzing CO_2RR for 5 h.

Table S7 Ag *K*-edge EXAFS fitting result. Structural parameters of different Cu_2O samples as well as reference samples extracted from the Cu *K*-edge EXAFS fitting.

Sample	Atomic scatter	No. of atoms (CN)	Interatomic distance (Å)	Debye-Waller factor (Å^2)	ΔE_0 (eV)	*R* factor
Cu-foil	Cu–Cu	12	2.53±0.03	0.009	3.8	0.002
Cu_2O	Cu–O	2	1.84±0.01	0.003	6.8	0.005
	Cu-Cu	12	3.05±0.02	0.023	11.0	
3DOP Cu_2O-CO	Cu–O	1.3	1.85±0.02	0.003	5.2	0.002
	Cu-Cu	10.5	3.04±0.04	0.025	8.5	
Cu_2O-CO	Cu-O	2	1.84±0.01	0.004	6.2	0.003
	Cu-Cu	12	3.03±0.02	0.022	7.1	
3DOP Cu_2O-CO-A	Cu–O	0.5	1.87±0.03	0.003	9.4	0.004
	Cu-Cu	5.4	2.55±0.01	0.007	6.0	
Cu_2O-CO-A	Cu–O	0.2	1.85±0.02	0.019	19.0	0.0002
	Cu-Cu	9.7	2.54±0.01	0.008	3.9	

S_0^2 is the amplitude reduction factor, S_0^2 = 0.85; CN is the coordination number; R is interatomic distance (the bond length between central atoms and surrounding coordination atoms); σ^2 is Debye-Waller factor (a measure of thermal and static disorder in absorber-scatterer distances); ΔE_0 is edge-energy shift (the difference between the zero kinetic energy value of the sample and that of the theoretical model). R factor is used to value the goodness of the fitting.

Note: 3DOP Cu_2O-CO-A and Cu_2O-CO-A represent the corresponding samples after electrocatalyzing CO_2R for 5 h.

References

[1] Shen, K.; Zhang, L.; Chen, X.; Liu, L.; Zhang, D.; Han, Y.; Chen, J.; Long, J.; Luque, R.; Li, Y.; Chen, B., Ordered macro-microporous metal-organic framework single crystals. *Science* **2018,** *359* (6372), 206-210.

[2] Zhang, D.-F.; Zhang, H.; Guo, L.; Zheng, K.; Han, X.-D.; Zhang, Z., Delicate control of crystallographic facet-oriented Cu_2O nanocrystals and the correlated adsorption ability. *Journal of Materials Chemistry* **2009,** *19* (29).

[3] Shi, X.; Shuai, Y.; Wang, F.; Zhang, C.; Cheng, Z. and Chen, X. J. Effects of ordered hierarchically porous structure on methane reforming performance in solar foam reacto. CO_2 Util. **2020**, 37, 147.

[4] Unver, A. A. and Himmelblau, D. M. Diffusion Coefficients of CO_2,C_2H_4, C_3H_6 and C_4H_8 in Water from 6°C to 65 °C *Journal of Chemical & Engineering Data* 1964,1964, 9, 428-431.

[5] Gilliam, R. J.; Graydon, J. W.; Kirk, D. W.; Thorpe, S. J., A review of specific conductivities of potassium hydroxide solutions for various concentrations and temperatures. *International Journal of Hydrogen Energy* 2007, *32* (3), 359-364.

[6] Gao, D.; Zegkinoglou, I.; Divins, N. J.; Scholten, F.; Sinev, I.; Grosse, P.; Roldan Cuenya, B., Plasma-Activated Copper Nanocube Catalysts for Efficient Carbon Dioxide Electroreduction to Hydrocarbons and Alcohols. *ACS Nano* **2017,** *11* (5), 4825-4831.

[7] Gao, Y.; Wu, Q.; Liang, X.; Wang, Z.; Zheng, Z.; Wang, P.; Liu, Y.; Dai, Y.; Whangbo, M. H.; Huang, B., Cu_2O Nanoparticles with Both [100] and [11] Facets for Enhancing the Selectivity and Activity of CO_2 Electroreduction to Ethylene. *Adv Sci* **2020,** *7* (6), 1902820.

[8] Liang, Z. Q.; Zhuang, T. T.; Seifitokaldani, A.; Li, J.; Huang, C. W.; Tan, C. S.; Li, Y.; De Luna, P.; Dinh, C. T.; Hu, Y.; Xiao, Q.; Hsieh, P. L.; Wang, Y.; Li, F.; Quintero-Bermudez, R.; Zhou, Y.; Chen, P.; Pang, Y.; Lo, S. C.; Chen, L. J.; Tan, H.; Xu, Z.; Zhao, S.; Sinton, D.; Sargent, E. H., Copper-on-nitride enhances the stable electrosynthesis of multi-carbon products from CO_2. *Nat Commun* **2018,** *9* (1), 3828.

[9] Fu, W.; Liu, Z.; Wang, T.; Liang, J.; Duan, S.; Xie, L.; Han, J.; Li, Q., Promoting C_{2+} Production from Electrochemical CO_2 Reduction on Shape-Controlled Cuprous Oxide Nanocrystals with High-Index Facets. *ACS Sustainable Chemistry & Engineering* **2020,** *8* (40), 15223-15229.

[10] Handoko, A. D.; Ong, C. W.; Huang, Y.; Lee, Z. G.; Lin, L.; Panetti, G. B.; Yeo, B. S., Mechanistic Insights into the Selective Electroreduction of Carbon Dioxide to Ethylene on Cu_2O-Derived Copper Catalysts. *The Journal of Physical Chemistry C* **2016,** *120* (36), 20058-20067.

[11] Moller, T.; Scholten, F.; Thanh, T. N.; Sinev, I.; Timoshenko, J.; Wang, X.; Jovanov, Z.; Gliech, M.; Roldan Cuenya, B.; Varela, A. S.; Strasser, P., Electrocatalytic CO_2 Reduction on CuO_x Nanocubes: Tracking the Evolution of Chemical State, Geometric Structure, and Catalytic Selectivity using Operando Spectroscopy. *Angew Chem Int Ed Engl* **2020,** *59* (41), 17974-17983.

[12] Wu, Z. Z.; Zhang, X. L.; Niu, Z. Z.; Gao, F. Y.; Yang, P. P.; Chi, L. P.; Shi, L.; Wei, W. S.; Liu, R.; Chen, Z.; Hu, S.; Zheng, X.; Gao, M. R., Identification of Cu(100)/Cu(111) Interfaces as Superior Active Sites for CO Dimerization During CO_2 Electroreduction. *J Am Chem Soc* **2022,** *144* (1), 259-269.

[13] Liu, C.; Zhang, M.; Li, J.; Xue, W.; Zheng, T.; Xia, C.; Zeng, J., Nanoconfinement Engineering over Hollow Multi-Shell Structured Copper towards Efficient Electrocatalytical C-C coupling. *Angew. Chem. Int. Ed.* ***2022****, 61, e202113498.*

[14] Yang, P. P.; Zhang, X. L.; Gao, F. Y.; Zheng, Y. R.; Niu, Z. Z.; Yu, X.; Liu, R.; Wu, Z. Z.; Qin, S.; Chi, L. P.; Duan, Y.; Ma, T.; Zheng, X. S.; Zhu, J. F.; Wang, H. J.; Gao, M. R.; Yu, S. H., Protecting Copper Oxidation State

via Intermediate Confinement for Selective CO_2 Electroreduction to C_{2+} Fuels. *J Am Chem Soc* **2020,** *142* (13), 6400-6408.

[15] Sikdar, N.; Junqueira, J. R. C.; Dieckhofer, S.; Quast, T.; Braun, M.; Song, Y.; Aiyappa, H. B.; Seisel, S.; Weidner, J.; Ohl, D.; Andronescu, C.; Schuhmann, W., A Metal-Organic Framework derived $Cu_xO_yC_z$ Catalyst for Electrochemical CO_2 Reduction and Impact of Local pH Change. *Angew Chem Int Ed Engl* **2021,** *60* (43), 23427-23434.

[16] De Luna, P.; Quintero-Bermudez, R.; Dinh, C.-T.; Ross, M. B.; Bushuyev, O. S.; Todorović, P.; Regier, T.; Kelley, S. O.; Yang, P.; Sargent, E. H., Catalyst electro-redeposition controls morphology and oxidation state for selective carbon dioxide reduction. *Nature Catalysis* **2018,** *1* (2), 103-110.

[17] Chen, C.; Li, Y.; Yu, S.; Louisia, S.; Jin, J.; Li, M.; Ross, M. B.; Yang, P., Cu-Ag Tandem Catalysts for High-Rate CO_2 Electrolysis toward Multicarbons. *Joule* **2020,** *4* (8), 1688-1699.

[18] Yao, K.; Li, J.; Wang, H.; Lu, R.; Yang, X.; Luo, M.; Wang, N.; Wang, Z.; Liu, C.; Jing, T.; Chen, S.; Cortes, E.; Maier, S. A.; Zhang, S.; Li, T.; Yu, Y.; Liu, Y.; Kang, X.; Liang, H., Mechanistic Insights into OC-COH Coupling in CO_2 Electroreduction on Fragmented Copper. *J Am Chem Soc* **2022,** *144* (31), 14005-14011.

[19] Sang, J.; Wei, P.; Liu, T.; Lv, H.; Ni, X.; Gao, D.; Zhang, J.; Li, H.; Zang, Y.; Yang, F.; Liu, Z.; Wang, G.; Bao, X., A Reconstructed $Cu_2P_2O_7$ Catalyst for Selective CO_2 Electroreduction to Multicarbon Products. *Angew Chem Int Ed Engl* **2022,** *61* (5), e202114238.

[20] Niu, Z. Z.; Gao, F. Y.; Zhang, X. L.; Yang, P. P.; Liu, R.; Chi, L. P.; Wu, Z. Z.; Qin, S.; Yu, X.; Gao, M. R., Hierarchical Copper with Inherent Hydrophobicity Mitigates Electrode Flooding for High-Rate CO_2 Electroreduction to Multicarbon Products. *J Am Chem Soc* **2021,** *143* (21), 8011-8021.

[21] Li, H.; Liu, T.; Wei, P.; Lin, L.; Gao, D.; Wang, G.; Bao, X., High-Rate CO_2 Electroreduction to C_{2+} Products over a Copper-Copper Iodide Catalyst. *Angew Chem Int Ed Engl* **2021,** *60* (26), 14329-14333.

[22] Lu, Y. F.; Dong, L. Z.; Liu, J.; Yang, R. X.; Liu, J. J.; Zhang, Y.; Zhang, L.; Wang, Y. R.; Li, S. L.; Lan, Y. Q., Predesign of Catalytically Active Sites via Stable Coordination Cluster Model System for Electroreduction of CO_2 to Ethylene. *Angew Chem Int Ed Engl* **2021,** *60* (50), 26210-26217.

[23] Wang, X.; Klingan, K.; Klingenhof, M.; Moller, T.; Ferreira de Araujo, J.; Martens, I.; Bagger, A.; Jiang, S.; Rossmeisl, J.; Dau, H.; Strasser, P., Morphology and mechanism of highly selective Cu(II) oxide nanosheet catalysts for carbon dioxide electroreduction. *Nat Commun* **2021,** *12* (1), 794.

[24] Zhao, Y.; Zu, X.; Chen, R.; Li, X.; Jiang, Y.; Wang, Z.; Wang, S.; Wu, Y.; Sun, Y.; Xie, Y., Industrial-Current-Density CO_2-to-C_{2+} Electroreduction by Anti-swelling Anion-Exchange Ionomer-Modified Oxide-Derived Cu Nanosheets. *J Am Chem Soc* **2022,** *144* (23), 10446-10454.

[25] Lv, J. J.; Jouny, M.; Luc, W.; Zhu, W.; Zhu, J. J.; Jiao, F., A Highly Porous Copper Electrocatalyst for Carbon Dioxide Reduction. *Adv Mater* 2018, 30 (49), e1803111.

[26] Wu, Y.; Chen, C.; Yan, X.; Liu, S.; Chu, M.; Wu, H.; Ma, J.; Han, B., Effect of the coordination environment of Cu in Cu_2O on the electroreduction of CO_2 to ethylene. *Green Chemistry* **2020,** *22* (19), 6340-6344.

[27] Kunze, S.; Tanase, L. C.; Prieto, M. J.; Grosse, P.; Scholten, F.; de Souza Caldas, L.; van Vorden, D.; Schmidt, T.; Cuenya, B. R., Plasma-assisted oxidation of Cu(100) and Cu(111). *Chem Sci* **2021,** *12* (42), 14241-14253.